ICES REPORT 14-20

August 2014

Fluid-Filled Fracture Propagation using a Phase-Field Approach and Coupling to a Reservoir Simulator

by

Thomas Wick, Gurpreet Singh, Mary F. Wheeler

The Institute for Computational Engineering and Sciences
The University of Texas at Austin
Austin, Texas 78712

Reference: Thomas Wick, Gurpreet Singh, Mary F. Wheeler , "Fluid-Filled Fracture Propagation using a Phase-Field Approach and Coupling to a Reservoir Simulator," ICES REPORT 14-20, The Institute for Computational Engineering and Sciences, The University of Texas at Austin, August 2014.

Fluid-Filled Fracture Propagation using a Phase-Field Approach and Coupling to a Reservoir Simulator

Thomas Wick Gurpreet Singh Mary F. Wheeler

July 31, 2014

Abstract

Tight gas and shale oil play an important role in energy security and in meeting an increasing energy demand. Hydraulic fracturing is a widely used technology for recovering these resources. A quantitative assessment of hydraulic fracturing jobs relies upon accurate predictions of fracture growth during slick water injection for single and multistage fracturing scenarios. It is also important to consistently model the underlying physical processes from hydraulic fracturing to long-term production. A recently introduced thermodynamically consistent phase-field approach for pressurized fractures in porous medium is utilized which captures several characteristic features of crack propagation such as joining, branching and non-planar propagation in heterogeneous porous media. This phase-field approach captures both the fracture-width evolution and the fracture-length propagation; here we address the latter. In this work, we briefly describe our phase-field fracture propagation model and then present a technique for coupling this to a fractured poroelastic reservoir simulator. The proposed coupling approach can be adapted to existing reservoir simulators. We presents two and three dimensional numerical tests to benchmark, compare and demonstrate the predictive capabilities of the fracture propagation model as well as the proposed coupling scheme.

Keywords. phase-field; pressurized fractures; iterative coupling algorithm; reservoir simulation

Introduction

Hydraulic fracturing is a well known method for recovering oil and gas from tight gas and shale plays. It is pivotal in meeting a continually growing energy demand. Concerns are also being raised regarding its impact on long and short term environmental implications. Thus, there is an imminent need for physically and mathematically consistent, accurate and robust computational models for representing fluid field fractures in a poroelastic medium. The simplest model description involves coupling of (1) mechanical deformation, (2) reservoir-fracture fluid flow, (3) and fracture propagation. The rock deformation is usually modeled using the linear elasticity theory (Biot (1941a,b, 1955)). For fluid flow modeling, lubrication theory and Darcy flow are assumed in the fracture and reservoir respectively, which are coupled through a leakage term. Finally, for fracture propagation the conventional energy-release rate approach of linear elastic fracture mechanics (LEFM) theory is used. We also note some of the concurring modeling and numerical approaches for fracture propagation currently used such as cohesive zone models (Xu and Needleman (1994)), displacement discontinuity methods (Crouch (1976)), partition-of-unity (Babuska and Belenk (1997)) based

XFEM/GFEM methods (Moes et al. (1999); de Borst et al. (2006); Secchi and Schrefler (2012); Babuska and Banerjee (2012)), boundary element formulations (BEM) (Castonguay et al. (2013)) and peridynamics (Silling (2000)).

Variational approaches (Francfort and Marigo (1998); Bourdin et al. (2008)) and a thermodynamically consistent phase field formulation (C. Miehe (2010)) have been employed in solid mechanics. An application to hydraulic fracturing is given in (Bourdin et al. (2012)). C. Miehe (2010) extended the variational approach (Francfort and Marigo (1998); Bourdin et al. (2008)) by modeling crack irreversibility through an entropy condition satisfying the second law of thermodynamics and decomposing the strain tensor to account for tension and compression. Our approach (Mikelić et al. (2013a,b)) is based upon C. Miehe (2010) with an extension to porous media applications where solids (geomechanics) interact with fluids. To develop a phase-field formulation for such applications, geomechanics and porous media flows are decoupled using fixed-stress splitting (Settari and Walters (2001); Mikelić and Wheeler (2012)). With this methodology, modeling and simulations of hydraulic fractures in poroelasticity have been considered (Mikelić et al. (2013a,b, 2014b); Wheeler et al. (2014); Mikelić et al. (2014a); Wick et al. (2014)).

We provide a brief recapitulation describing Griffith's model for fracture growth in brittle media. The classical theorem of minimum energy suggests that an equilibrium state achieved by an elastic body deformed by surface forces is such that the potential energy of the system is minimal. This was later augmented by Griffith (1921), in his seminal work, assuming a different equilibrium state is possible which accounts for formation of fractures as a mechanism for lowering potential energy. This criterion of rupture assumes that the cohesive forces, due to molecular attraction, act close to the fracture tip. Thus, the contribution of cohesive forces (surface potential energy) to the total potential energy can be assumed to be negligible. Based upon these assumptions, a decrease in potential energy is proportional to the generated surface area with the critical energy release rate (G_c) as the constant of proportionality. In this work, we rely upon this classical work along with its assumptions on the fracture growth criteria. As noted by Barenblatt (1962), we do not underestimate the significance of cohesive forces at the fracture tip. However, the contribution of these forces to the total potential energy is assumed to be significant only during fracture nucleation which diminishes as the fracture grows. Based upon these arguments we assume that LFEM is applicable.

Using a phase-field approach, a lower-dimensional crack surface is approximated as a diffusive transition zone by a phase-field function φ. **Fig. 1** shows this diffusive transition zone (also brittle or mushy-zone) between the broken (white zone) and the unbroken (brown zone) states of the material. A fixed-topology finite element phase-field approach is shown where a (lower-dimensional) crack is approximated with the help of a phase-field function. The phase-field function is an indicator function with values 0 and 1 inside and outside the crack, respectively. The mushy-zone also provides a smooth interpolation for the interface between a fracture and reservoir. A coupling of reservoir fluids and geomechanics allows a comprehensive study of this multiscale problem where only few results have been published to date (see for instance Dean and Schmidt (2008) and Lujun and Settari (2007)). Further, we also describe an algorithm to integrate fracture growth patterns with our reservoir simulator IPARS (Implicit Parallel Accurate Reservoir Simulator). This allows for both short term transient pressure analysis and long term recovery predictions. We note that crack or

fracture propagation, which will be used interchangeably, implies both variation of fracture width (or aperture) **and** its length.

The major advantages of using phase-field modeling for crack propagation are four-fold: First, and most important, the model is easy to implement and uses a fixed-grid topology in which remeshing for resolving the exact fracture location is avoided. Second, fracture nucleation, propagation, kinking, and curvilinear path are intrinsically determined. This avoids computational overheads associated with post-processing of quantities such as stress intensity factors. Third, we can easily handle large fracture networks since complex phenomena of joining and branching does not require keeping track of fracture interfaces. Fourth, modeling crack growth in heterogeneous media does not require special treatment. Here however, the length-scale parameter ε should be chosen accordingly. Additionally, the crack opening displacement (fracture aperture) can be calculated using the phase-field function. We use the pressurized crack propagation model in a poroelastic medium using a phase-field approach proposed by Mikelić et al. (2013a,b).

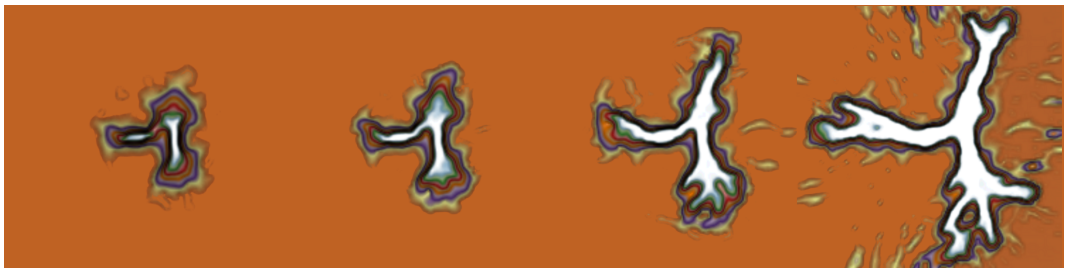

Figure 1: Evolution of two pressurized fractures: first joining, then nonplanar growth and finally branching in heterogeneous porous media.

Our focus in this paper is on the following aspects. We investigate the previously described phase-field approach for different crack propagation scenarios including heterogeneous porous media including permeability and geomechanical parameters. Second, we perform detailed studies of multi-stage fractures. Third, we consider the phase-field model as a fractured-well approach in a reservoir and we consequently couple this approach to a reservoir simulator. This paper concentrates primarily on the approach for fracture growth using slick-water injection. We account for varying reservoir complexities such as natural fractures, faults and barriers using a comprehensive fractured poroelastic reservoir flow model. This allows for a two-stage production optimization owing to (1) a well-engineered hydraulic fracturing scheme followed by (2) an optimal fractured well placement considering far from well-bore reservoir complexities. The paper is organized as follows: we first provide our motivation for the work and the reason for our choice of using a phase-field model for hydraulic fracturing. In the next section, we provide the governing equations for the fracture phase-field approach the reservoir flow equations. In the section after, we provide details on the coupling algorithm between the fracture phase-field model and the reservoir simulator. In the final section, numerical tests are discussed to demonstrate our method.

Pressurized and Fluid-filled Crack Propagation Models using Phase-field

In this section, we describe the proposed model development starting by defining a two-field problem in two unknowns: (1) a vector displacement field and (2) a scalar phase-field variable (φ), assuming a known pressure field (the so-called pressurized fracture propagation). This is later extended to a three-field problem, adding scalar pressure (p) as an unknown, accounting for flow inside the porous rock matrix and the fracture (the so-called fluid-filled fracture propagation). Therein, a single pressure diffraction equation (see Mikelić et al. (2014a)), derived from the mass conservation equation and Darcy's law, is used for local flow field calculations. The elasticity and phase-field equations are formulated as an energy minimization problem. We obtain a weak form of the differential equations by differentiating this energy minimization function with respect to the solution variables. This serves as a natural setting for using a Galerkin finite element method for spatial discretization. Before we begin, it is important to discuss the key features of the classical brittle fracture theory (Griffith (1921)) used in this work. The theory postulates two physical phenomena: (1) linear elasticity and (2) fracture propagation, as energy dissipation mechanisms, strictly separated by a threshold (critical energy release rate) assuming a sharp transition between the fractured and non-fractured media. The Griffith's criterion for brittle fracture propagation assumes:

1. The crack growth is irreversible.
2. The energy release rate is bounded above by a critical energy release rate.
3. The crack grows if and only if the energy release rate is critical.

Let Ω be the reservoir domain, as shown in **Fig. 2**, with the fracture $\mathcal{C} \subset \Omega$.

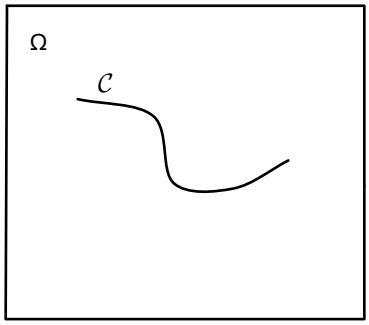

Figure 2: Problem description.

Pressurized fracture propagation model (two-field problem) We begin by describing the pressurized fracture approach where a known pressure field is assumed on the domain Ω. The pressure remains invariant along the fracture length varying only temporally based upon a simple correlation. The pressure variation along the fracture length is assumed to be negligible. Later we show that this assumption is valid if the fracture conductivity is

substantially larger than the reservoir conductivity, which is usually the case. The energy functional for a poroelastic material (Ω) with a crack ($\mathcal{C}$) reads:

$$E(u,\mathcal{C}) = \underbrace{\frac{1}{2}\int_{\Omega}\sigma_E : e(u)}_{\text{Elastic energy}} - \underbrace{\int_{\Omega}\alpha_B(p-p_0)\nabla\cdot u}_{\text{Pore pressure contribution}} + \underbrace{G_c\mathcal{H}^{d-1}(\mathcal{C})}_{\text{Fracture energy}}, \tag{1}$$

with the following constitutive stress-strain equation and definition of strain $e(u)$:

$$\sigma_E = 2\mu e(u) + \lambda tr(e(u))I, \tag{2}$$

$$e(u) = \frac{1}{2}(\nabla u + \nabla u^T). \tag{3}$$

where μ and λ denote the Lamé parameters, σ_E the Cauchy stress tensor, $e(u)$ the strain tensor, α_B the Biot coefficient, p the pore pressure, p_o the reference pressure, u the displacements. G_c is the critical elastic energy release rate depending on the material and is determined experimentally and $\mathcal{H}^{d-1}$ is the length of the fracture. Please note that G_c is related to stress intensity factor under certain assumptions on the material such as an isotropic, linear elastic solid (Irwin (1958)). Further, we follow the approach presented by Ambrosio and Tortorelli (1990) for approximating the fracture length ($\mathcal{H}^{d-1}$) using an elliptic functional

$$\frac{1}{2\varepsilon}\|1-\varphi\|^2 + \frac{\varepsilon}{2}\|\nabla\varphi\|^2, \tag{4}$$

thereby introducing an additional variable φ, referred to as the phase-field variable hereafter. This variable is a quantity defined on the entire domain Ω for a time span varying from 0 to T. A careful examination of **Eqn. 4** shows, for a given value of $\varepsilon > 0$, this functional assumes lowest values when φ is a constant assuming values of either 0 (fracture) or 1 (porous rock matrix). We notice that the phase-field approach is related to gradient-type material modeling with a characteristic length-scale. Here, the above regularization parameter ε can be considered as such a length-scale parameter that has a physical meaning (Pham et al. (2011); C. Miehe (2010) and references cited therein). The second term ensures that φ changes smoothly between 0 and 1 allowing the representation of the fracture as a diffuse interface. **Eqn. 4** represents a mathematically-consistent approximation of the *true* crack $\mathcal{H}^{d-1}$.

In order to satisfy assumptions 2 and 3 the energy functional (**Eqn. 1**) is regularized with φ as follows:

$$\begin{aligned} E_\varepsilon(u,\varphi) = \frac{1}{2}\int_{\Omega}((1-\kappa)\varphi_+^2 + \kappa)\sigma_E : e(u) - \int_{\Omega}\alpha_B(p-p_0)\varphi_+^2\nabla\cdot u \\ + G_c\left(\frac{1}{2\varepsilon}\|1-\varphi\|^2 + \frac{\varepsilon}{2}\|\nabla\varphi\|^2\right) \end{aligned} \tag{5}$$

Here, φ_+ is the maximum of φ and 0, $\kappa \approx 0$ (determined by machine precision) is a positive regularization parameter for the elastic energy and the length-scale parameter ε denotes the width of the transition zone in which φ changes from 0 to 1 (this width is illustrated as the

contour lines between the white and brown regions in **Fig. 1**). One can see from **Eqn. 5** that if φ is 0 (fracture), the first and second terms become zero and the energy functional is dominated by the critical energy release rate G_c. Similarly when φ is 1, the third term becomes zero. An intermediate behavior can be seen for values between 0 and 1. Finally, we impose the irreversibility constraint (assumption (1)) on φ; i.e.,

$$\partial_t \varphi \leq 0, \tag{6}$$

which ensures that the state variables change in the direction of energy minimization or entropy maximization, in accord with the 2^{nd} law of thermodynamics. Then, the final energy functional reads:

$$\begin{aligned} E_\varepsilon(u,\varphi) = \frac{1}{2}\int_\Omega ((1-\kappa)\varphi_+^2 + \kappa)\sigma_E : e(u) - \frac{1}{2}\int_\Omega \alpha_B(p-p_0)\varphi_+^2 \nabla\cdot u \\ + G_c\left(\frac{1}{2\varepsilon}\|1-\varphi\|^2 + \frac{\varepsilon}{2}\|\nabla\varphi\|^2\right) + I_{K(\varphi^{n-1})}(\varphi), \end{aligned} \tag{7}$$

where the last term $I_{K(\varphi^{n-1})}(\varphi^n)$ is a penalization term to impose the irreversibility constraint (6). We are now ready to derive differential equations in a Galerkin fashion that can be easily adapted and implemented in legacy reservoir simulators using finite element discretizations. For the sake of brevity, we directly introduce these differential equations. The reader is referred to Mikelić et al. (2013a) for a detailed derivation. The problem statement then reads: Find u and φ such that,

$$\int_\Omega \left((1-\kappa)\varphi_+^2 + \kappa\right)\mathcal{G}e(\eta) : e(w) - \int_\Omega (\alpha_B - 1)(\varphi_+^2 p \text{div } w) + \int_\Omega \varphi_+^2 \nabla p w = 0$$
$$\forall \text{ admissible test functions } w,$$

as well as,

$$\begin{aligned} \int_\Omega (1-\kappa)(\varphi_+ \mathcal{G}e(\eta) : e(\eta)\psi - \int_\Omega 2(\alpha_B - 1)(\varphi_+ \, p \text{ div } \eta)\psi + 2\int_\Omega \varphi_+ \nabla p \, \eta\psi \\ + G_c\Big(-\int_\Omega \frac{1}{\varepsilon}(1-\varphi)\psi + \int_\Omega \varepsilon\nabla\varphi\nabla\psi\Big) + \int_\Omega (\Xi + \gamma(\varphi - \varphi^{n-1}))^+\psi = 0 \\ \forall \text{ admissible test functions } \psi. \end{aligned}$$

Here, Ξ and γ are a penalization function and parameter, respectively, to enforce the irreversibility constraint of crack growth with the help of an augmented Lagrangian formulation (Wheeler et al. (2014)). In the last term, φ^{n-1} denotes the phase-field solution to the previous time step.

Fluid-filled fracture propagation model (three-field problem) In the previous section, a given uniform fracture pressure was assumed for crack propagation. Here we briefly describe an extension of this approach where a pressure field is computed by solving a flow problem on the entire domain (both reservoir and fracture). An extended Reynold's lubrication equation and Darcy's law are solved in the fracture and reservoir domains, respectively along with the fluid mass conservation equations. The benefit of our proposed approach is that both sets of equations have similar structure identified by the phase-field variable as separate fracture ($\Omega_F(t)$) and reservoir ($\Omega_R(t)$) domains. Here, $\Omega_F(t)$ is the volume approximation of the crack $\mathcal{C}$. For further details the reader is referred to Mikelić et al. (2014a). The mass conservation equations for fluid flow are:

$$\begin{aligned} \partial_t \rho_F + \nabla \cdot (\rho_F v_F) &= q_F - q_L \quad \text{in } \Omega_F(t), \\ \partial_t (\rho_R \phi_R) + \nabla \cdot (\rho_R v_R) &= q_R \quad \text{in } \Omega_R(t). \end{aligned} \tag{8}$$

Please note that the fracture porosity is set to one. The fracture volume is accounted for by the spatial discretization. Here, the velocities are defined by the Reynold's lubrication equation and Darcy's law for the fracture and the reservoir, respectively:

$$v_j = -\frac{K_j}{\nu_j}(\nabla p_j - \rho_j g). \tag{9}$$

The term q_L represents the leakage from the fracture owing to the 3D approximation of 2D Reynold's lubrication equation for the fracture domain. Where, $j = F, R$ denotes the fracture and reservoir domains, ϕ_j the fluid fraction, K_j the permeability tensor, ν_j and ρ_j the fluid viscosity and density, respectively, g the gravity and q_j the source/sink term. A comparison of Darcy's law and Reynold's lubrication equation shows that $K_F = \frac{w(u)^2}{12\mu}$, where $w(u)$ is the fracture width (or aperture) calculated from jump in normal displacements u. A detailed derivation of our leakage term can be found in Mikelić et al. (2014a).

Discretization and solution algorithm The flow and mechanics equations are solved using the fixed-stress iterative coupling scheme (Settari and Walters (2001); Mikelić and Wheeler (2012)) where decoupling is achieved as illustrated in Figure 3 along with the algorithmic flow chart 1. We then first discretize in time using a backward Euler scheme followed by spatial discretization with a continuous Galerkin finite element method on a hexahedral grid with grid size parameter h. Here, all variables are discretized by continuous bilinears in space. We note that $h \ll \varepsilon$, which requires fine meshes around the fracture(s). To this end, we use local mesh refinement with hanging nodes (see Figure 4).

Algorithm 1 Augmented Lagrangian fixed-stress solution algorithm

For each time t^n
repeat
  Solve augmented Lagrangian loop (outer loop)
  repeat
    Solve two-field fixed-stress (inner loop):
      Solve the pressure diffraction Problem (8)
      Solve linear elasticity in Problem (8)
  until Stopping criterion

$$\max\{\|u^l - u^{l-1}\|, \|p^l - p^{l-1}\|\} \leq \mathrm{TOL}_{\mathrm{FS}}, \quad \mathrm{TOL}_{\mathrm{FS}} > 0$$

  for fixed-stress split is satisfied
  Solve the nonlinear phase-field in Problem (8)
  Update

$$\Xi_{k+1} = (\Xi_k + \gamma(\varphi_{k+1} - \varphi^{n-1}))_+, \quad k = 0, 1, 2, \ldots$$

until Stopping criterion

$$\|\Xi_{k-1} - \Xi_k\| \leq \mathrm{TOL}_{\mathrm{AL}}, \quad \mathrm{TOL}_{\mathrm{AL}} > 0$$

is satisfied
Set: $(u^n, \varphi^n) := (u_k, \varphi_k)$.
Increment $t^n \to t^{n+1}$.

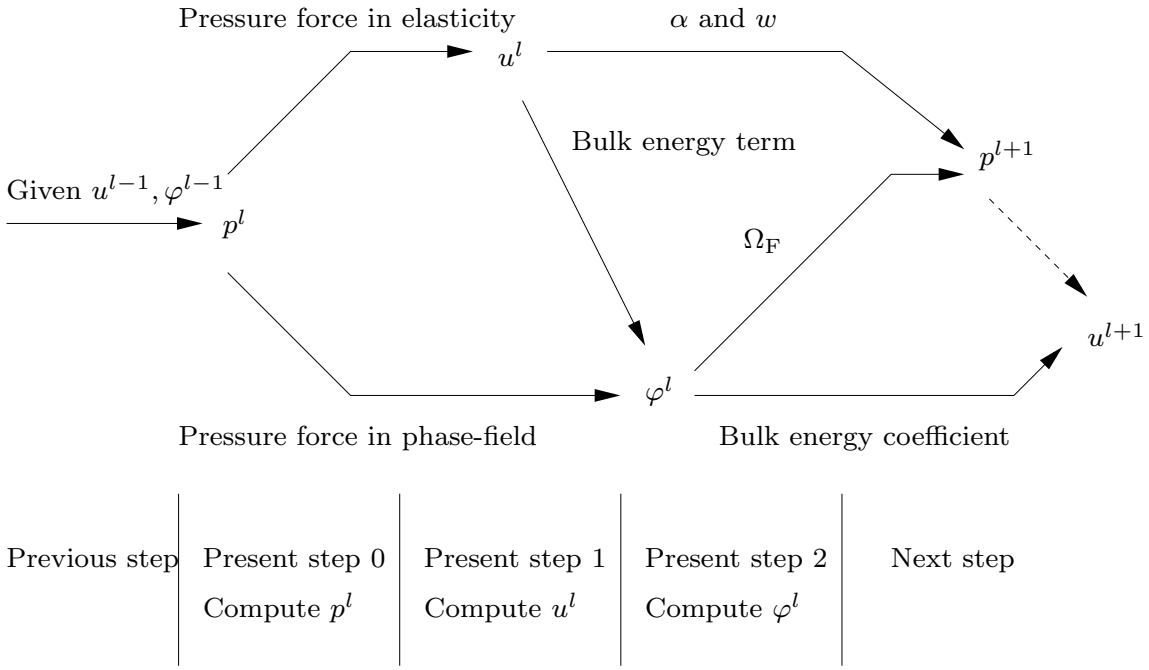

Figure 3: Explication how the three equations for pressure, displacements and phase-field couple together. In each iteration step (within each time step), we compute first p^l, then u^l, and finally φ^l, where each variable influences the other two. Specifically, φ^l alters the fracture domain Ω_{F}, which influences the computation of the new pressure p^{l+1}.

Integrating Phase-field Crack Propagation and Fractured Reservoir Flow Models

In this section, we describe the proposed coupling method while outlining a work-flow for translating fracture location, geometry and width information between the phase-field crack propagation model and the production reservoir code. The use of hexahedral elements for spatial discretization in both models allows translation of fracture location and variables from one model to another. The phase-field with crack growth and localized flow is used as a pre-processor step for the fractured reservoir flow. This results in a forward solution with the pertinent fracture geometry and width translated at the end of the propagation. We consider phase-field as an independent module that can be coupled to other codes. This assumes hydraulic fracture growth to be a local or near well bore phenomenon which is not affected by far-field reservoir complexities such as reservoir boundaries, faults and barriers. Under this assumption, the two processes: hydraulic fracturing and later production are decoupled. Thus a local flow problem with appropriate boundary conditions is solved to compute a local pressure field during fracture propagation.

This forward coupling is computationally inexpensive and adequately captures local flow field variations effecting fracture growth. Another advantage is that the phase field crack propagation model generates fracture growth information as a standalone module. The spatial and temporal scales associated with fracture growth and later production from a hydraulically fractured reservoir are widely different. Therefore, it is reasonable to treat the two processes separately. As discussed previously, the phase-field model includes a localized

fluid flow description and can therefore generate crack growth information as a stand alone. We then post-process and adapt this crack geometry data for our fractured poroelastic reservoir simulator resulting in a one-way coupling. This approach can be adapted for other legacy reservoir simulators.

Projection of variables/ mesh reconstruction We start with the phase-field approach and solve for p, u, φ. At the end of the fracturing process, the reservoir simulator needs the pressure p as initial pressure, φ to detect the shape of the fracture and finally the width $w := w(u)$, which is computed as jump of the normal displacements. The shape of the fracture is determined for all $\varphi < thr$, where thr denotes a certain threshold, say $thr = 0.1$ (see Figure 4). If $\varphi < thr$ in a cell, it is marked as fracture cell. All unknown quantities are computed at cell centers with the associated co-ordinate information to the reservoir simulator.

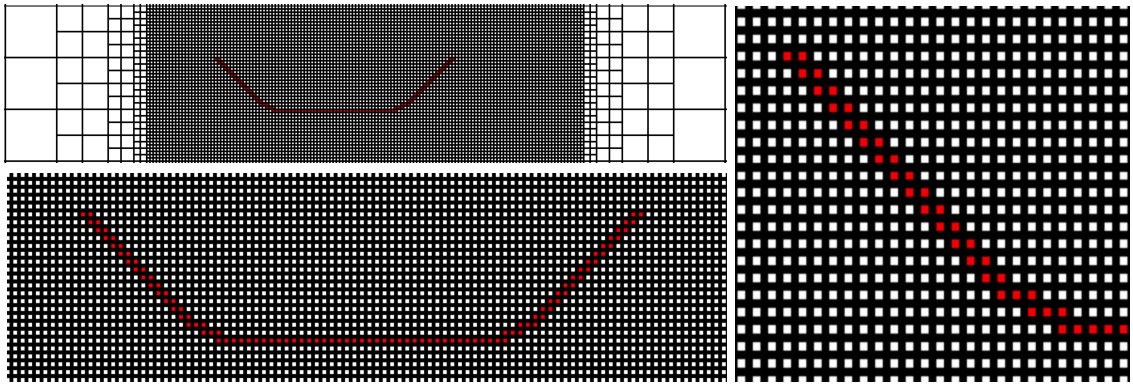

Figure 4: Determination of crack shape using threshold of the phase field variable to determine fracture cells (marked red). The phase-field module uses locally-refined grids with hanging nodes, which allows to reduce the computational cost significantly.

We post-process and adapt fracture geometry from crack growth model for the fractured poroelastic reservoir flow model. **Fig. 5** shows reconstruction of a coarse, locally distorted, hexahedral mesh which adequately captures the three characteristic length scale variations of a typical elliptic fracture.

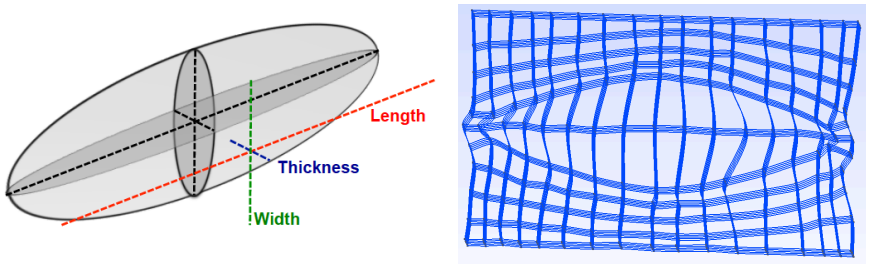

Figure 5: Reconstructing the fracture geometry.

Fig. 6 outlines a work-flow for reconstructing 3D fracture geometry, for reservoir flow

simulation, from 2D fracture information generated by the fracture growth model. The first row shows geometry information for one and three fractures (left and right, respectively) in the YZ plane. A typical fracture growth pattern, in the XZ plane is then used to reconstruct 3D fracture geometries. We use the fact that final fracture geometries after slick water injection are strongly correlated to reservoir rock property data and can therefore be scaled.

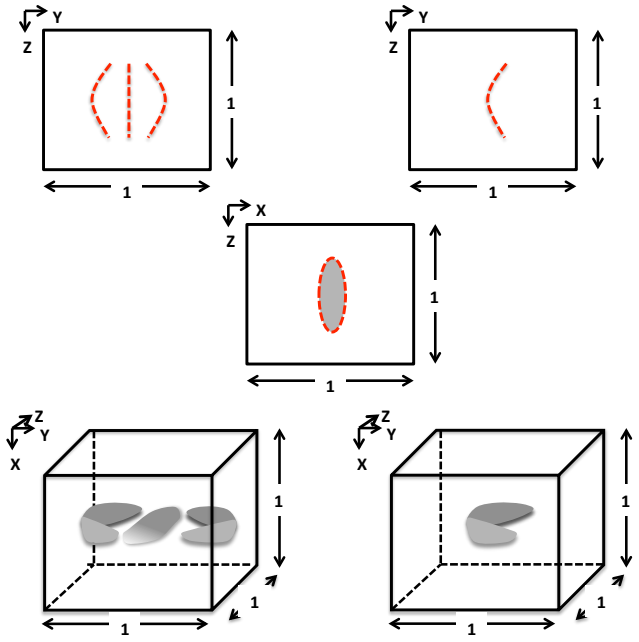

Figure 6: Work-flow for reconstructing 3D fracture geometry from 2D information.

Fractured well model As previously described, the crack propagation model already couples fracture flow to reservoir and is therefore complete in itself. That means, starting with a given setting, we commence with that model and compute a fracture geometry, which might include curvilinear growth, branching and joining. The fracture geometry is passed to the reservoir simulator, as described in the previous section. The width and the pressure information from the phase-field model are set as the initial conditions for the reservoir simulator. **Fig. 7** (right) shows fractured well placement (red blocks) in a reservoir with natural fractures (shaded orange). The mesh adaption is convenient since both models utilize hexahedral meshes thus avoiding computationally costly interpolation between meshes with different mesh elements (tetrahedral, prisms etc.).

The key advantage of our suggested ideas is concerned with the effort in coupling. Rather than iterating in each time step between both frameworks, the phase-field is used as a preprocessor step and as such acts as a own module. This allows us to run different well placement scenarios with the reservoir simulator using the same fracture geometry avoiding redundant fracture growth calculations for each scenario. The accuracy of the phase-field approach for modeling fracture propagation increases, as the mesh is refined. The spatial and temporal scales associated with crack propagation are much smaller when compared to

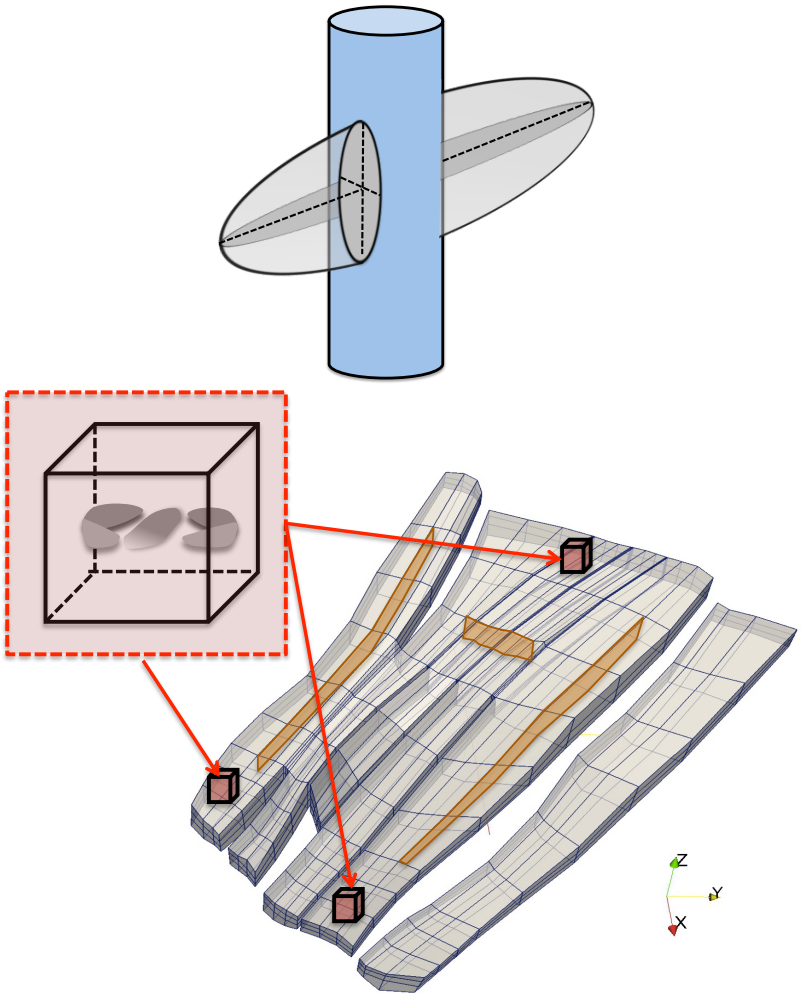

Figure 7: Integrating fractures generated by phase field model as a fractured well model.

reservoir flow. Therefore, the use of a fine mesh for fracture growth computations followed by reservoir flow calculations on a coarse mesh is computationally efficient. In order to expedite the calculations for the phase-field fracture growth model, we utilize a dynamic mesh refinement approach with locally refined grids and hanging nodes (see **Fig. 4**). For example, if we run 20 time steps, we perform the first 15 on a coarse mesh and refine the last 5 time steps to get more accurate fracture tip and associated variable information. This procedure keeps the computational cost very reasonable while increasing accuracy.

Numerical Tests

We illustrate our methodology by several numerical tests in two and three dimensions. First, we highlight the capabilities of the fractured-well phase-field model and present some crack propagation scenarios including multi-stage fractures, stress-shadowing effects and crack growth in heterogeneous porous media with nonplanar fractures. Second, we use one of these scenarios, extract the fracture and run the reservoir simulator.

The fracture-well phase-field model is computed with the multiphysics template (Wick (2013)) in combination with deal.II's (Bangerth et al. (2012)) step-31 for the usage of two different degree-of-freedom-handlers to build an iterative solution algorithm as needed for the fixed-stress splitting. In the following, we provide geometry information and parameters for the test cases.

Geometry, grid and time step parameters

The computational domain for all 2d tests is $\Omega = (0,4)^2$. Here, two fractures each with length 1 and midpoints $x = 1.5$ and $x = 2.5$ are prescribed. In the second test, the distance is enlarged and the midpoints are $x = 1$ and $x = 3$. In the cases of the three multi-stage fractures, we consider the midpoints $x = 1, 2, 3$. Here, in the first test all three fractures have length 1, in the second test the middle fracture has length 0.5 and in the final test 1.5. In 3d, in the cube $\Omega = (0,10)^3$, we prescribe a two penny-shape cracks with radius $r = 1.0$ in the $y = 5.0$-plane with mid-points $(5.0, 3.0, 5.0)$ and $(5.0, 7.0, 5.0)$. The crack is approximated as a volume by extending it with the spatial discretization parameter h in up- and downward y-direction, respectively (for details, we refer the reader to Wheeler et al. (2014)). As boundary conditions we set the displacements zero on $\partial\Omega$. We compute 50 (2d) and 50 (3d) time steps with time step size $\Delta t = 0.01$ (2d) and $\Delta t = 0.005$ (3d), respectively. We note that the characteristic fracture time scale is,

$$T_F = \frac{L^2 \eta_F c_F}{\tilde{K}_F} = \frac{1 \times 10^{-3} \times 10^{-8}}{10^{-8}} = 10^{-3},$$

in which we assumed a characteristic fracture length 1 and characteristic fracture permeability $\tilde{K}_F = 10^{-4}$.

Model parameters

The augmented Lagrangian penalization parameter is $\gamma = 10^4$ (2d) and $\gamma = 10^3$ (3d). Several parameters and geometry-related issues depend on the spatial mesh size parameter h. Namely, for the regularization parameters we choose the relations $\kappa = 10^{-6} \times h, \varepsilon = 2h = 0.088$ (2d) and $\kappa = 10^{-6} \times h, \varepsilon = 2h = 1.09$ (3d).

Flow parameters In all examples, the gravity g is set to zero and the fluid is only driven by the point source injection q. We inject fluid at a constant rate into the fractures. In 2d and 3d, we use $q = 1$. Furthermore, the permeability in the reservoir is $K_R = 10^{-12}$. In the the second example, Test 2, we use a randomly varying permeability between 5×10^{-12} and 10^{-13}. Next, $M = 2.5 \times 10^{-8}$, $c_F = 10^{-8}$, $\nu_R = \nu_F = 1.0 \times 10^{-3}$, $\rho_R^0 = \rho_F^0 = 1$. Regarding the Biot coefficient, we perform computations with $\alpha = 0$ because it has been shown in Mikelić et al. (2014a) that $\alpha = 0$ and $\alpha = 1$ yield the same crack patterns if the characteristic time scale of the fracture is taken into account.

Elasticity and phase-field parameters

The fracture toughness is chosen as $G_c = 1.0$. The mechanical parameters are $\mu = 4.2 \times 10^7$ and $\lambda = 2.8 \times 10^7$. In the second example, we employ randomly varying Lamé parameters $\mu = 4.2 \times 10^6 - 9.4 \times 10^7$ and $\lambda = 2.6 \times 10^6 - 9.3 \times 10^7$.

Comparing fracture propagation in 3D and 2D domains In this example, we first show a numerical experiment simulating simultaneous propagation of two penny-shaped fractures in a 3D domain. This is followed by a 2D experiment, in a similar setting, to compare 2D and 3D results. **Fig. 8** shows fracture patterns during growth at T = 0, 15 and 25 seconds for the 3D case. Similarly, **Fig. 9** shows fracture locations at T = 0, 20 and 30 seconds for the 2D case.

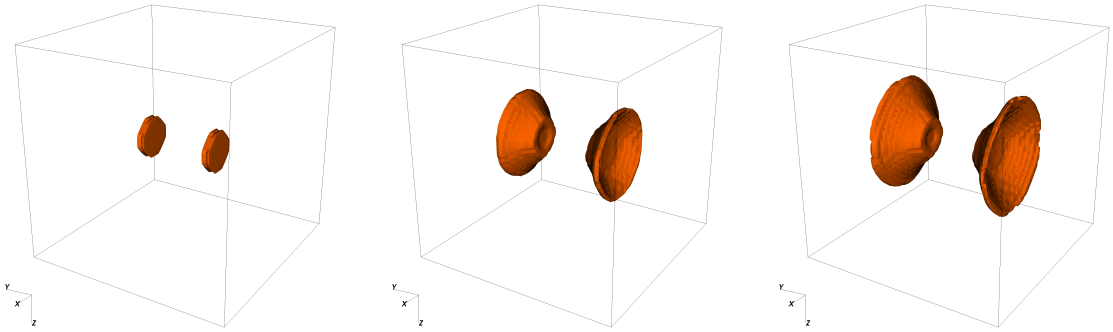

Figure 8: Crack pattern for simultaneous propagation of two penny-shaped fractures at T= 0, 15 and 25 seconds in 3D domain.

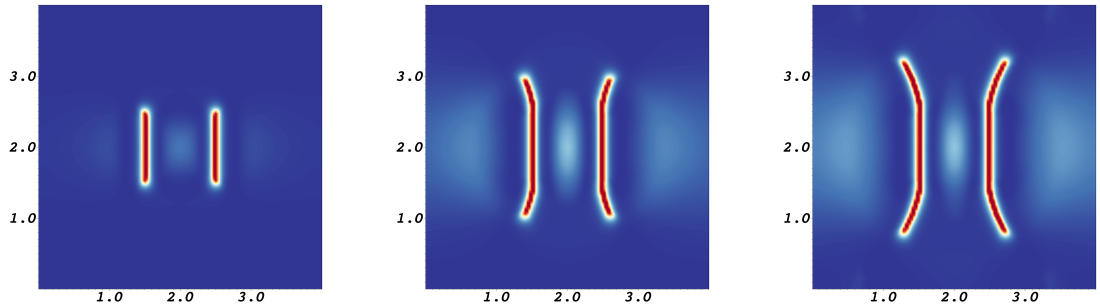

Figure 9: Crack pattern for simultaneous propagation of two fractures at T=0, 20 and 30 seconds in a 2D domain.

Since the two cases presented here are symmetrical the temporal variation of pressures at the centers of the two fractures, for each case, are similar. **Fig. 10** shows the time evolution of pressure at the center of one of the fractures for the 3D (left) and 2D (right) domains. Note that the pressure builds up to threshold value and then starts dropping as the fracture starts growing. The results show resemblance of the fracture growth and

transient pressure for the 3D and 2D cases.

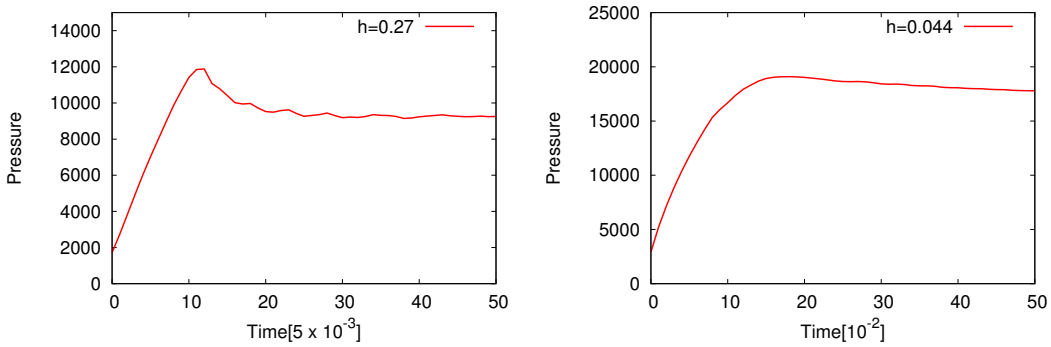

Figure 10: Transient pressure at the center of the fractures for 3D (left) and 2D (right) cases.

Effect of fracture spacing on fracture growth In this section, we present a numerical experiment, similar to the 2D case presented earlier, with a larger initial fracture spacing and studying the resulting effect on the fracture pattern. The fracture locations at time T = 0, 20 and 20 seconds are shown in **Fig. 11**. It can be observed by comparing **Figs. 10** and **11** that as the spacing is reduced the fracture pattern becomes diverging. This result demonstrates that an optimal fracture spacing can be achieved which maximizes reservoir fracture interface area and therefore productivity.

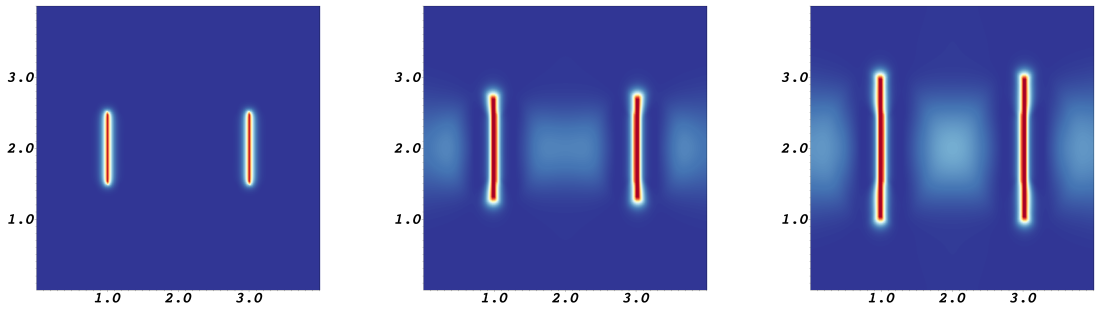

Figure 11: Crack pattern for simultaneous propagation of two fractures, with larger spacing, at T=0, 20 and 30 seconds.

Effect of discrete fractures on fracture growth In this example, we study the effect of an existing fracture on the propagation of another fracture. This setting is devised to provide insight into growth patterns for sequential hydraulic fracturing. In **Fig. 12** the left fracture is stationary whereas the right fracture grows due to injection of hydraulic fluids. The stationary fracture (left) is given a higher material stiffness property compared to the reservoir in order to replicate a propped fracture. As it can be seen, the hydraulic fracture does not show considerable pattern change due to the presence of an adjacent discrete fracture. Although a more detailed study can be conducted to evaluate the combined effect of orientation, we restrict ourselves to the case of parallel fracture for the sake of brevity. **Fig. 13** shows the stress fields (Frobenius norm) at times T = 0, 20 and 40 seconds.

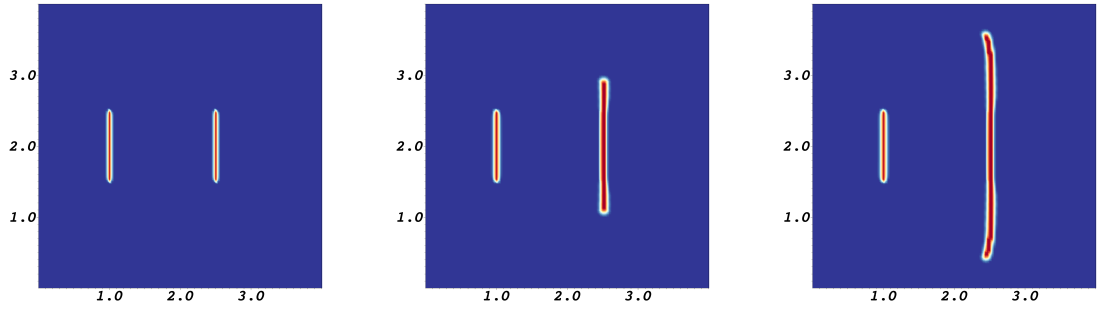

Figure 12: Crack pattern for sequential hydraulic fracturing at T=0, 20 and 40 seconds.

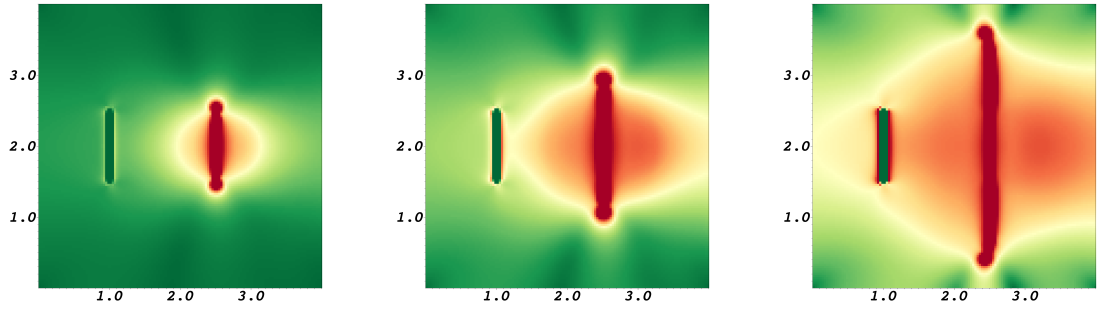

Figure 13: Stress field for sequential hydraulic fracturing at T=0, 20 and 40 seconds.

Effect of heterogeneity on fracture growth In this set of tests, we extend the case of two simultaneous fracture propagation in a 2D domain to a heterogeneous porous media **Fig. 15** and non-constant reservoir permeabilities **Fig. 16**. **Fig. 15** and **Fig. 16** show fracture growth with branching and joining for different times.

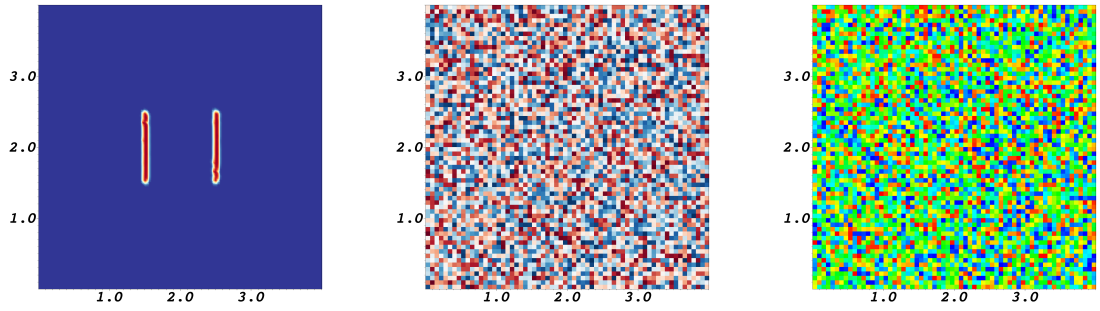

Figure 14: Initial crack pattern (left), randomly distributed Lamé coefficients (middle) and non-constant permeability (right). In the two latter figures, red denotes high values and blue/green low values.

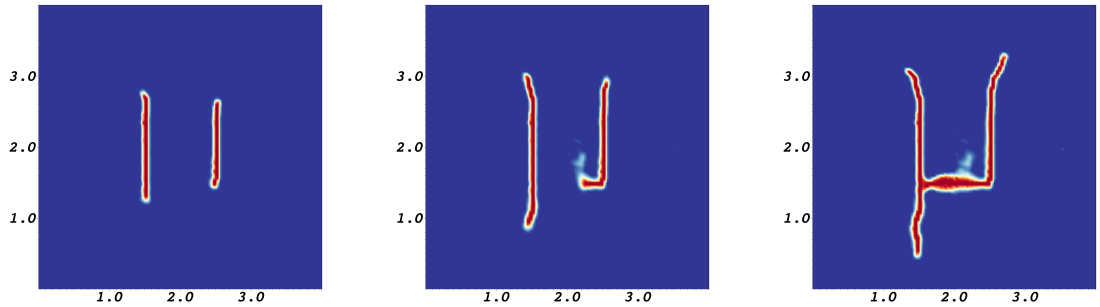

Figure 15: Crack pattern for fracture propagation in a heterogeneous medium at $T = 20, 30, 50$ seconds.

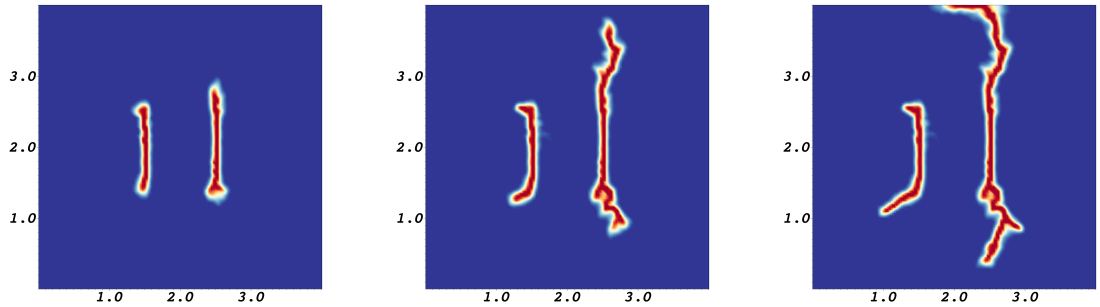

Figure 16: Crack pattern for fracture propagation in a heterogeneous medium and non-constant permeability at $T = 5, 10$ and 15 seconds.

Effect of stress shadowing on fracture growth Here, we investigate the effect of stress-shadowing and initial fracture nucleation lengths on fracture growth for simultaneous propagation of three fractures. The material properties (Lameé parameters) are kept homogenous to accentuate observations and are by no means restrictive. Three cases were considered: a) equal fracture nucleation lengths (**Fig. 17**), b) shorter nucleation length for middle fracture (**Fig. 19**) and c) longer nucleation length for middle fracture (**Fig. 21**). Please note that although boundary conditions play an important role in fracture growth the emphasis here is solely on fracture-fracture interaction.

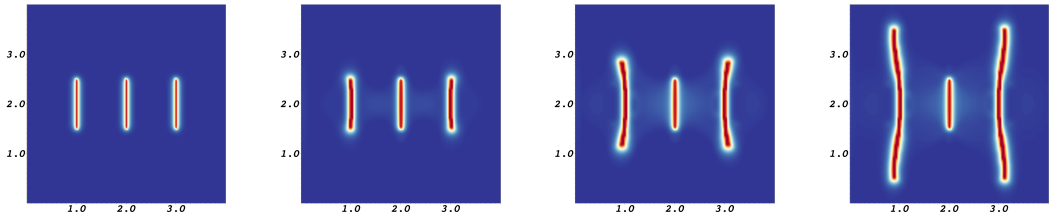

Figure 17: Example 3, Test 1, crack pattern at $T = 0, 20, 30, 50$.

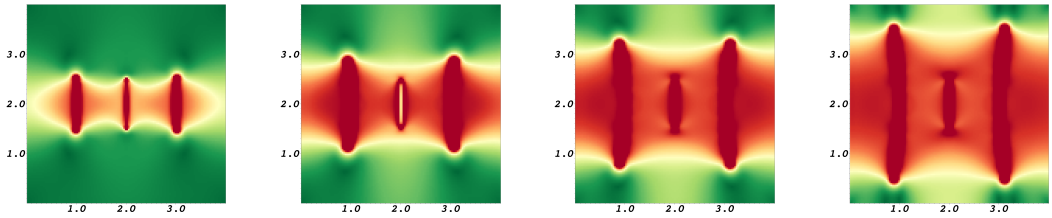

Figure 18: Example 3, Test 2, stress distribution at $T = 0, 20, 30, 50$.

Figs. 18, 20 and, **22** show the stress-fields (Frobenius norm) for the aforementioned three cases. In, **Fig. 17** we observe that the growth of the middle fracture is shunned due to the stress shadowing from the outer two fractures. Similar behavior is observed for the case with shorter nucleation length for middle fracture. However, the case with longer nucleation length for middle fracture shows contrasting behavior. Here the stress shadow owing to the middle fracture shuns the growth of outer fractures. This numerical test shows that a careful evaluation of stress shadowing effects is pivotal for planning a hydraulic fracturing job, beginning from perforation to propagation using slick water injection.

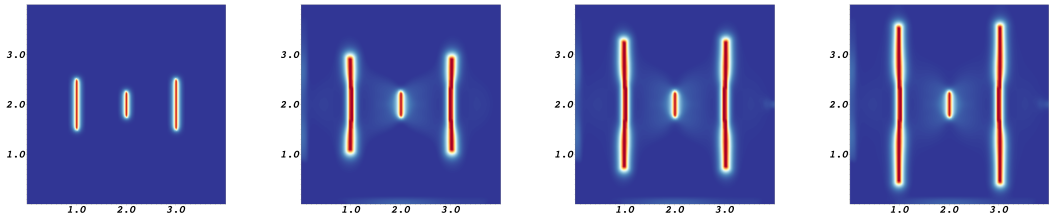

Figure 19: Example 3, Test 2, crack pattern at $T = 0, 20, 30, 50$.

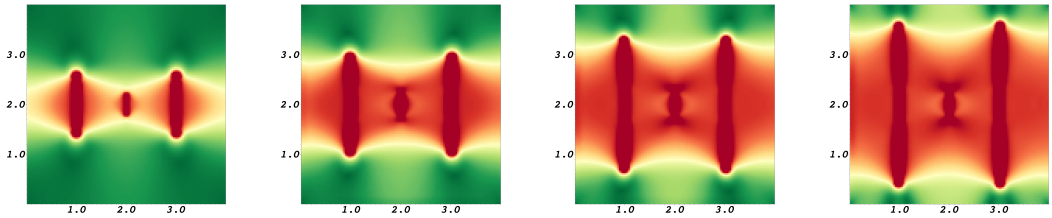

Figure 20: Example 3, Test 2, stress distribution at $T = 0, 20, 30, 50$.

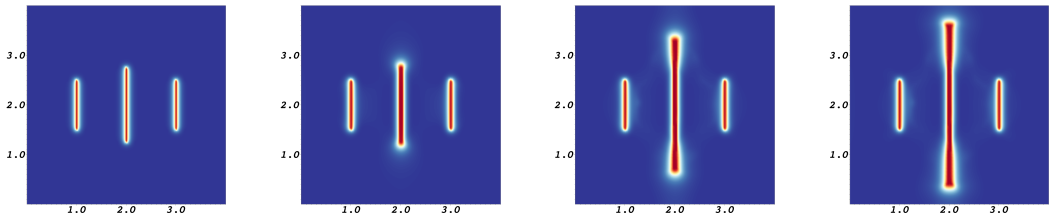

Figure 21: Example 3, Test 3, crack pattern at $T = 0, 20, 30, 50$.

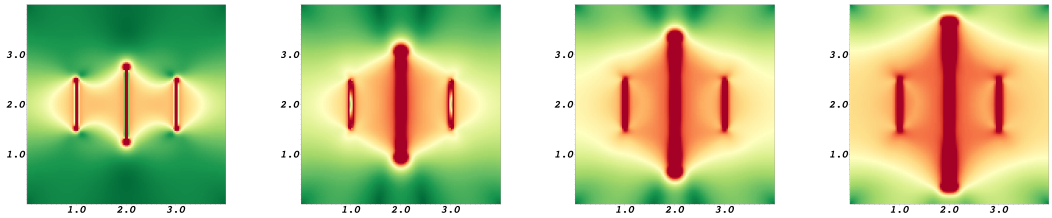

Figure 22: Example 3, Test 3, stress distribution at $T = 0, 20, 30, 50$.

TABLE 1—Reservoir properties, Multistage fractures			
ϕ	0.15-0.22	$K_x \neq K_y = K_z$	0-3800 mD
c_w	1.E-7 psi^{-1}	c_o	1.E-4 psi^{-1}
ρ_w	62.4 lbm/ft^3	ρ_o	56 lbm/ft^3
ν_w	1 cP	ν_o	2 cP
S_w^0	0.31	P_w^0	1500 psi

Coupling the phase-field model to a reservoir simulator: a fractured well-bore model In this section, we present an example to demonstrate the aforementioned approach for an explicit coupling of fracture growth to a reservoir simulator based upon general hexahedral discretization. A synthetic case is generated from Brugge field geometry (see e.g. Peters et al. (2009); Chen et al. (2010)) where the wells are augmented with hydraulic fractures. Here the use of fractured wells reduces the number of injection wells while improving sweep efficiency. The phase field fracture propagation model, followed by production evaluation of reservoir, allows us to develop an intuitive understanding of recovery predictions and serves as a decision making tool for design, evaluation and long term field developments.

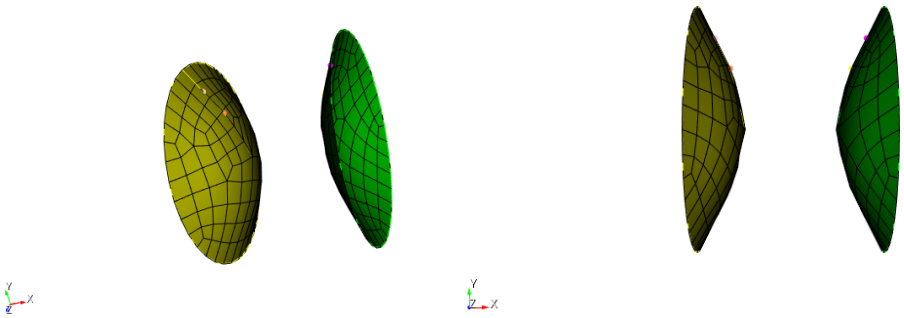

Figure 23: Coarse fracture mesh after adaptation.

Although not restrictive, for the sake of simplicity, we consider the fracture pattern as shown in **Fig. 8**. The geometry information from the phase field fracture propagation model is post-processed and adapted to obtain a coarser mesh while maintaining mesh quality. This reduces time-step size restrictions and numerical errors associated with mesh elements. **Fig. 23** shows the reconstructed, coarse, structured fracture mesh with quadrilateral (hexahedral in 3D) elements. This fracture pattern is integrated with a well-bore model and is used as a fractured well model in our reservoir simulator IPARS.

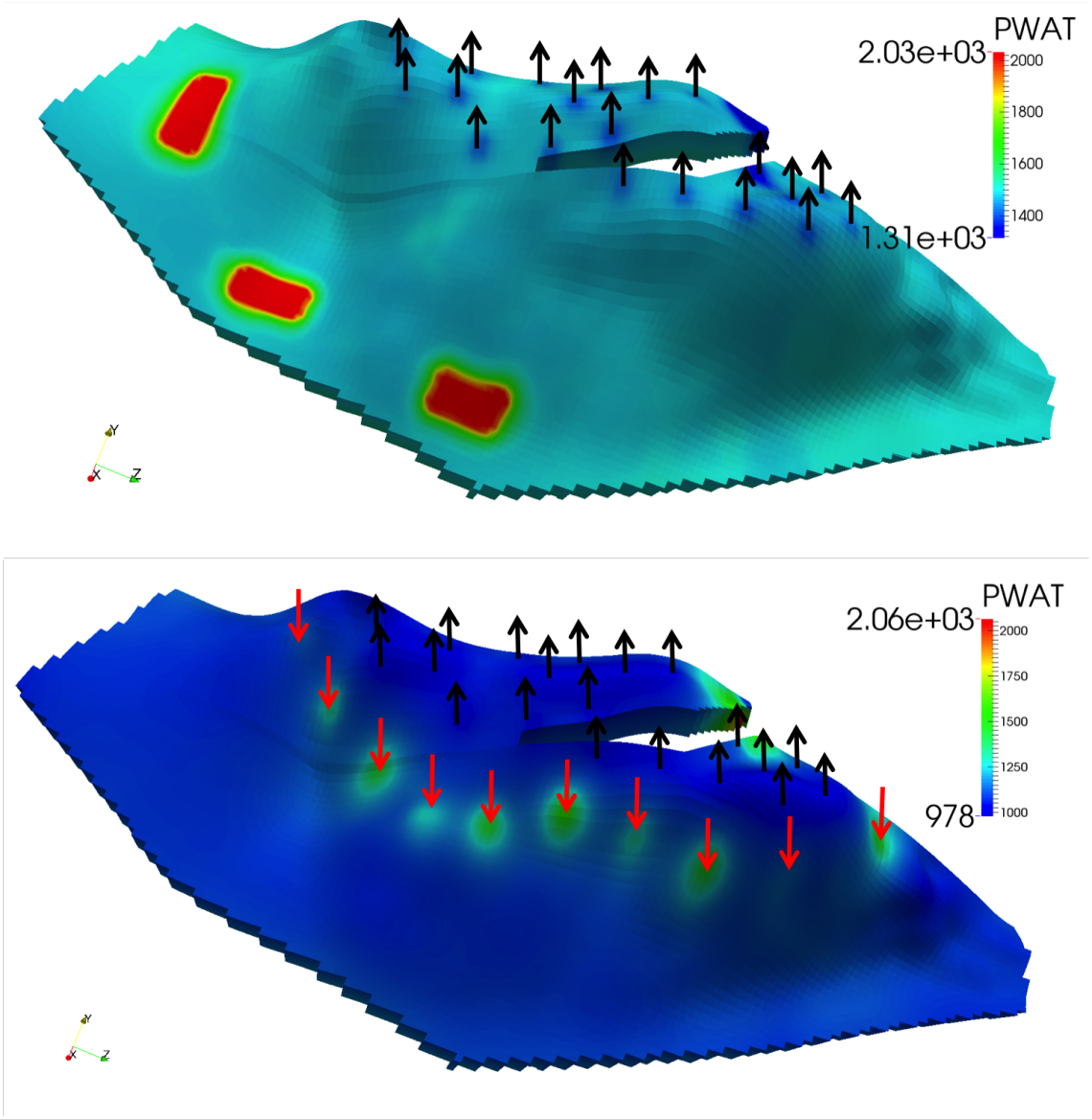

Figure 24: Brugge field geometry with fractured injection wells (top) and original Brugge field case (bottom).

Table 1 provides material and fluid properties required for solving flow and geomechanics. The values presented in the table provide typical values used for this simulation run. **Fig. 24** (left) shows the fractured Brugge field geometry with 20 bottom-hole pressure specified production wells at 1000 psi. Here a pressure profile after 2 days is used to aid in visualizing the location of the fractured injection wells. The three red regions show the hydraulically fractured, injection wells with a bottom-hole pressure specification of 2600 psi. The original Brugge field case is shown in **Fig. 24** (right) with 30 bottom-hole pressure specified wells with 10 injectors at 2600 psi and 20 producers at 1000 psi where injectors are located at a higher elevation compared to the producers. The distorted reservoir ge-

ometry and fractures are captured using 9×48×139 general hexahedral elements and then discretized using a MFMFE scheme (Singh et al. (2014)). **Fig. 25** displays permeability fields in the X (left) and Y (right) directions. The Z direction permeability is equal to the Y direction permeability.

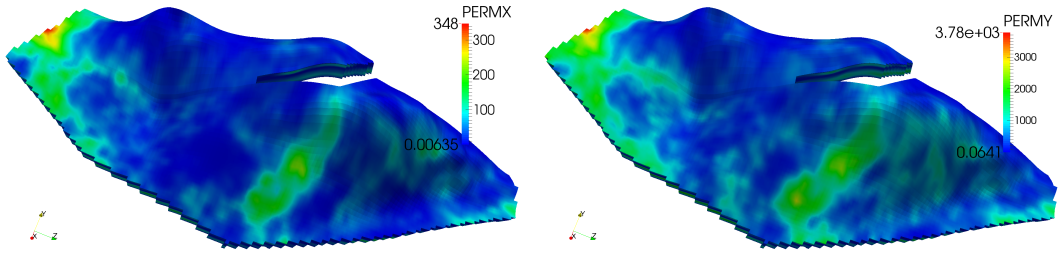

Figure 25: X (left) and Y (right) direction permeability fields.

Fig. 26 shows pressure (left) and saturation (right) profiles at the end of 1000 days. The fractured injection wells are placed at greater depths compared to production wells so that the gravity assists in oil recovery. A comparison between the pressure and saturation profiles for the two cases show that a lower number of fractured wells are required for improved sweep efficiencies compared to conventional wells.

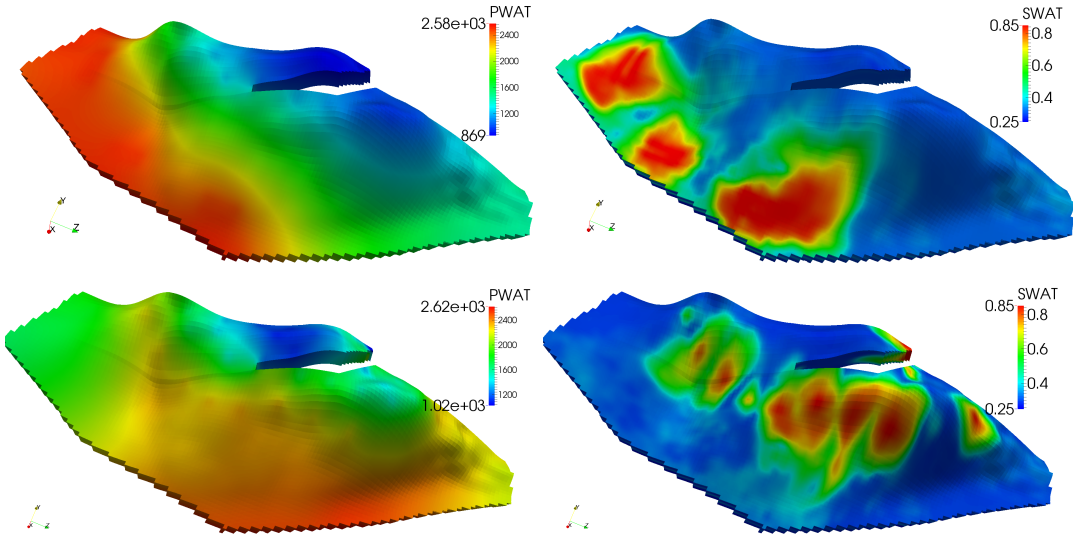

Figure 26: Pressure (left) and saturation (right) profiles after 1000 days for fractured (top) and original (bottom) Brugge field cases.

Conclusions

In this work, we first presented a fracture propagation model and its numerical solution scheme for treating slick water hydraulic fracturing based on a phase-field approach. This adequately describes crack propagation and associated pressure variation during growth. First, this phase-field model is employed to compute various fracture propagation scenarios in two and three dimensions and crack growth in an anisotropic, heterogeneous, poroelastic medium. In particular, the pressure profile shows a buildup until a critical energy rate is reached resulting in fracture growth. Second, we successfully coupled this phase-field approach with a reservoir simulator. The integration is based on a computationally efficient one-way coupling which allows the use of the phase-field approach as a pre-processor step. With our proposed approach we are able to simulate hydraulic fracturing and production stages. An extension to black-oil and compositional models for the reservoir flow description can also be achieved.

Nomenclature

$\Omega =$	reservoir domain
$\mathcal{C} =$	fracture domain
$E(u, \mathcal{C}) =$	energy functional
$\sigma_E =$	stress tensor
$e(u) =$	strain tensor
$\alpha_B =$	Biot coefficient
$p =$	fluid pressure
$p_0 =$	reference pressure
$u =$	displacement vector
$G_c =$	critical energy release rate
$\mathcal{H}^{d-1}(\mathcal{C}) =$	length of fracture, Hausdroff measure
$\mu, \lambda =$	Lamé parameters
$\nu =$	fluid viscosity
$I =$	identity tensor
$\varphi =$	phase field variable
$\kappa, \varepsilon =$	regularization parameters
$w(u) =$	fracture aperture or width
$K =$	absolutre permeability
$\rho =$	fluid density
$g =$	acceleration due to gravity
$q_{F,R} =$	source/sink for fracture (F) or reservoir (R)
$q^L =$	fracture leakage term

Acknowledgments

This research was funded by ConocoPhillips grant UTA10-000444, DOE grant ER25617, Saudi Aramco grant UTA11-000320 and Statoil grant UTA13-000884. In addition, the first author has been supported by an ICES postdoctoral fellowship and a Humboldt Feodor Lynen fellowship. The authors would like to express their sincere thanks for the funding.

References

Ambrosio, L. and Tortorelli, V., 1990. Approximation of Functionals Depending on Jumps by Elliptic Functionals via Gamma-Convergence. *Communications on Pure and Applied Mathematics*, **43** (8): 999–1036.

Babuska, I. and Banerjee, U., 2012. Stable generalized finite element method (sgfem). *Comput. Methods Appl. Mech. Engrg.*, **201-204**: 91–111.

Babuska, I. and Belenk, J., 1997. The partition of unity method. *Int. J. Numer. Methods Engrg.*, **40**: 727–758.

Bangerth, W., Heister, T., Kanschat, G., et al., 2012. *Differential Equations Analysis Library.*

Barenblatt, G. I., 1962. The mathematical theory of equilibrium cracks in brittle fracture. *Advances in applied mechanics*, **7** (1).

Biot, M., 1941a. Consolidation settlement under a rectangular load distribution. *J. Appl. Phys.*, **12** (5): 426–430.

Biot, M., 1941b. General theory of three-dimensional consolidation. *J. Appl. Phys.*, **12** (2): 155–164.

Biot, M., 1955. Theory of elasticity and consolidation for a porous anisotropic solid. *J. Appl. Phys.*, **25**: 182–185.

Bourdin, B., Chukwudozie, C., and Yoshioka, K., 2012. A variational approach to the numerical simulation of hydraulic fracturing. SPE Journal, Conference Paper 159154-MS.

Bourdin, B., Francfort, G., and Marigo, J.-J., 2008. The variational approach to fracture. *J. Elasticity*, **91** (1–3): 1–148.

C. Miehe, M. H., F. Welschinger, 2010. Thermodynamically consistent phase-field models of fracture: variational principles and multi-field fe implementations. *International Journal of Numerical Methods in Engineering*, **83**: 1273–1311.

Castonguay, S., Mear, M., Dean, R., and Schmidt, J., 2013. Predictions of the growth of multiple interacting hydraulic fractures in three dimensions. SPE Journal, Conference Paper 166259-MS.

Chen, C., Wang, Y., and Li, G., 2010. Closed-loop reservoir management on the brugge test case. *Computational Geosciences*, **14**: 691–703.

Crouch, S., 1976. Solution of plane elastic problem by the displacements discontinuity method. *Int. J. Num. Meth. in Eng.*, **10**: 301–343.

de Borst, R., Rethoré, J., and Abellan, M., 2006. A numerical approach for arbitrary cracks in a fluid-saturated porous medium. *Arch. Appl. Mech.*, **75**: 595–606.

Dean, R. H. and Schmidt, J., 2008. Hydraulic fracture predictions with a fully coupled geomechanical reservoir simulator. SPE Journal, Conference Paper 116470-MS.

Francfort, G. A. and Marigo, J.-J., 1998. Revisiting brittle fracture as an energy minimization problem. *J. Mech. Phys. Solids*, **46** (8): 1319–1342.

Griffith, A. A., 1921. The Phenomena of Rupture and Flow in Solids. *Philosophical Transactions of the Royal Society of London. Series A, Containing Papers of a Mathematical or Physical Character*, **221**: 163–198.

Irwin, G., 1958. Elastizität und plastizität. Handbuch der Physik, Editor: S. Flügge, Bd. 6.

Lujun, J. and Settari, A., 2007. A novel hydraulic fracturing model fully coupled with geomechanics and reservoir simulator. SPE Journal, Conference Paper 110845-MS.

Mikelić, A., Wheeler, M., and Wick, T., 2013a. A phase-field approach to the fluid filled fracture surrounded by a poroelastic medium. ICES-Preprint 13-15.

Mikelić, A., Wheeler, M., and Wick, T., 2013b. A quasi-static phase-field approach to the fluid filled fracture. ICES-Preprint 13-22.

Mikelić, A., Wheeler, M., and Wick, T., 2014a. A phase-field method for propagating fluid-filled fractures coupled to a surrounding porous medium. ICES Report 14-08.

Mikelić, A., Wheeler, M., and Wick, T., 2014b. Phase-field modeling of pressurized fractures in a poroelastic medium. ICES-Preprint 14-18.

Mikelić, A. and Wheeler, M. F., 2012. Convergence of iterative coupling for coupled flow and geomechanics. *Comput Geosci*, **17** (3): 455–462.

Moes, N., Dolbow, J., and Belytschko, T., 1999. A finite element method for crack growth without remeshing. *Int. J. Numer. Methods Engrg.*, **46**: 131–150.

Peters, E., Arts, R., Brouwer, G., and Geel, C., 2009. Results of the Brugge benchmark study for flooding optimisation and history matching. *SPE 119094-MS. SPE Reservoir Simulation Symposium.*

Pham, K., Amor, H., Marigo, J.-J., and Maurini, C., 2011. Gradient Damage Models and Their Use to Approximate Brittle Fracture. *Int. J. of Damage Mech.*, 1–36.

Secchi, S. and Schrefler, B. A., 2012. A method for 3-d hydraulic fracturing simulation. *Int J Fract*, **178**: 245–258.

Settari, A. and Walters, D. A., 2001. Advances in coupled geomechanical and reservoir modeling with applications to reservoir compaction. *SPE Journal*, **6** (3): 334–342.

Silling, S. A., 2000. Reformulation of elasticity theory for discontinuities and long-range forces. *Journal of the Mechanics and Physics of Solids*, **48** (1): 175–209.

Singh, G., Wick, T., Wheeler, M., Pencheva, G., and Kumar, K., 2014. Impact of accurate fractured reservoir flow modeling on recovery predictions. SPE 188630-MS, SPE Hydraulic Fracturing Technology Conference, Woodlands, TX.

Wheeler, M., Wick, T., and Wollner, W., 2014. An augmented-Lagangrian method for the phase-field approach for pressurized fractures. *Comp. Meth. Appl. Mech. Engrg.*, **271**: 69–85.

Wick, T., 2013. Solving monolithic fluid-structure interaction problems in arbitrary Lagrangian Eulerian coordinates with the deal.ii library. *Archive of Numerical Software*, **1**: 1–19. URL `http://www.archnumsoft.org`.

Wick, T., Singh, G., and Wheeler, M., 2014. Pressurized fracture propagation using a phase-field approach coupled to a reservoir simulator. SPE 168597-MS, SPE Hydraulic Fracturing Technology Conference, Woodlands, TX.

Xu, X. and Needleman, A., 1994. Numerical simulations of fast crack growth in brittle solids. *Journal of the Mechanics and Physics of Solids*, **42**: 1397–1434.